



Influence of convergent plate boundaries on upper mantle flow and implications for seismic anisotropy

Julian P. Lowman

Department of Physical and Environmental Sciences, University of Toronto Scarborough, 1265 Military Trail, Toronto, Ontario, M1C 1A4, Canada (lowman@utsc.utoronto.ca)

Also at Department of Physics, University of Toronto, Toronto, Ontario, Canada M5S 1A7

Laura T. Pinero-Feliciangeli

Paseo Los Ilustres, Instituto de Ciencias de la Tierra, Facultad de Ciencias, Universidad Central de Venezuela, Los Chaguaramos, Caracas, Venezuela 1010-A

J.-Michael Kendall

Department of Earth Sciences, University of Bristol, Wills Memorial Building, Queen's Road, Bristol, BS8 1RJ UK

M. Hosein Shahnas

Department of Physical and Environmental Sciences, University of Toronto Scarborough, 1265 Military Trail, Toronto, Ontario, M1C 1A4, Canada

Also at Department of Physics, University of Toronto, Toronto, Ontario, Canada M5S 1A7

[1] Shear-wave splitting observations in the region of the upper mantle enveloping subduction zones have been interpreted as showing extensive regions of trench-parallel flow, despite the difficulty of reconciling such behavior with a sound model based on the forces that drive mantle motion. To gain insight into the observations, we systematically investigate flow patterns around the cold downwelling sheets associated with consumed plate material in a three-dimensional numerical mantle convection model. First, we compare results from calculations employing prescribed plate geometries and kinematic plate velocities where the convergent plate boundary morphology is varied while keeping the plate velocity and convective parameters fixed. Subsequently, we examine the flow around sheet-like downwellings in a number of convection calculations featuring dynamically evolving plate velocities. All of the calculations include thick viscous plates and a stratified mantle viscosity. In all of the models examined, we find that at mid-upper mantle depths, flow directions no longer align with plate motion and the influence of buoyancy-driven downwellings clearly dominates flow solutions. In the first models analyzed, a pair of plates are included in the calculations, and the large-scale flow is generally roll-like. In the final model we investigate the interaction of four plates and a plate geometry characterized by triple junctions. We examine a sequence from this calculation that features a triple junction of convergent boundaries. In this model, large-scale flow characterized by convection rolls is superseded by a complex flow solution where flow in the mid-upper mantle neither aligns uniformly with the plate motion nor necessarily follows the forcing associated with local buoyancy sources. In this setting, upper mantle flow in the vicinity of the sheet-like downwellings featured in the solution moves orthogonal, obliquely, and even parallel to different sections

of the convergent plate boundaries. In the latter case our calculations of the deformation of a fixed volume parcel of upper mantle material suggest that an olivine lattice-preferred orientation should develop that would result in a fast polarizing direction for seismic shear waves parallel to the slab. Our findings have implications for the interpretation of flow in the upper mantle based on seismic anisotropy.

Components: 11,727 words, 16 figures, 1 table.

Keywords: mantle; convection; seismic; anisotropy; plate; slab.

Index Terms: 8120 Tectonophysics: Dynamics of lithosphere and mantle: general (1213); 7208 Seismology: Mantle (1212, 1213, 8124); 7240 Seismology: Subduction zones (1207, 1219, 1240).

Received 13 March 2007; **Revised** 11 June 2007; **Accepted** 19 June 2007; **Published** 10 August 2007.

Lowman, J. P., L. T. Pinero-Feliciangeli, J.-M. Kendall, and M. H. Shahnas (2007), Influence of convergent plate boundaries on upper mantle flow and implications for seismic anisotropy, *Geochem. Geophys. Geosyst.*, 8, Q08007, doi:10.1029/2007GC001627.

1. Introduction

[2] Interpretations of shear-wave splitting data from numerous subduction regions have been used to support arguments that mantle flow may be deflected by the relative horizontal translation of strong slabs [e.g., *Savage, 1999; Russo and Silver, 1994*]. However, because it is the dense subducted plates which are the greatest source of buoyancy driving the mantle flow it is hard to conceive a dynamically based argument that would explain what forces would cause mantle flow to deflect around a cold slab. The possibilities appear to be that either our understanding of the translation between seismic observations and flow direction by mineral physics is incomplete or that mantle flow is not as predictable as simple 2D models may suggest and that regions of trench parallel flow may exist in confined or broad regions. The latter explanation does not suggest that the mantle can flow around slabs but instead concedes that the superposition of numerous buoyancy sources in 3D space may allow flow to run parallel to a slab on one side of a subduction zone in some settings.

[3] Early examination of subduction zone dynamics used 2-D corner flow models to explain mantle flow in the vicinity of subduction zones [e.g., *Ribe, 1989*]. However, anisotropy observations from subduction regions around the world have suggested that the mantle flow in these areas is complex and three-dimensional [*Savage, 1999; Russo and Silver, 1994; Fouch and Fischer, 1996*]. Some authors have proposed that trench-parallel mantle flow might develop in convergent settings due to retrograde motion of the slab or slab rollback [*Alvarez, 1992; Russo and Silver, 1994; Yu and Park, 1994*]. This type of flow has been

simulated in physical analog experiments [*Buttles and Olson, 1998*]. Numerical calculations have attempted to link the flow field to such shear-wave splitting observations by imposing a trench-parallel component in the flow velocity in subduction models [*Hall et al., 2000*].

[4] Inherent in understanding the connection between the seismic observations and flow in the mantle is a thorough understanding of the response of the minerals in the mantle to applied forces. Indeed, a large body of work exists in the literature that is dedicated to determining the relationship between seismic anisotropy and flow direction [*Ribe, 1989; Blackman et al., 1996; Tommasi, 1998; Chastel et al., 1993; Blackman and Kendall, 2002; Kaminski and Ribe, 2001*]. Laboratory studies have shown that in regimes dominated by deformation mechanisms of dislocation creep, and under moderate to large strains, the *a* axis of olivine will become aligned in the direction of mantle flow [*Zhang and Karato, 1995*].

[5] Whatever the response of seismic anisotropy to the fabric of upper mantle minerals may be in the conditions relevant to subduction zones, the seismic observations suggest that flow in some regions is moving parallel to the convergent plate boundary because the orientation of the fast direction for shear-wave splitting is variable. For example, the western Pacific is characterized by plate boundary segments exhibiting fast regions running both parallel and orthogonal to subduction zones [*Fouch and Fischer, 1996; Sandvol and Ni, 1997*]. Consequently, in this work we are motivated to examine dynamic models that allow for the coexistence of regions featuring trench parallel and trench orthogonal flow in the same solution.

[6] Gaining insight into the nature of the flow patterns in the upper mantle in subduction zone settings requires high resolution 3D mantle convection models incorporating model plates. In addition, calculations need to feature the appropriate heating conditions and mantle viscosity structure. The models presented in this work allow for complex arrangements of upper mantle slab segments to form either as a natural consequence of the calculation evolution, or alternatively, because of the combination of plate motion and plate geometry prescribed. We use the versatility of the model to first investigate flow in calculations with prescribed conditions and then to investigate flow in calculations with dynamically determined time-dependent plate motion. Our goal is to investigate the hypothesis that the superposition of various sources of buoyancy in a 3D geometry may in some situations allow for regions of flow moving parallel to a cold sheet in the upper mantle over limited or even extensive regions. If such regions exist and if they feature stretching of mantle material in the direction parallel to the adjacent downwelling then they could give rise to trench parallel polarization of fast splitting S waves.

2. Model Description

[7] We use the 3D numerical mantle convection model MC3D to model the influence of plate motion on fully developed, 3D Cartesian geometry, thermal convection in an infinite Prandtl number Boussinesq fluid [e.g., Gable *et al.*, 1991; Lowman *et al.*, 2003]. We assume a Newtonian depth-dependent viscosity and allow for the inclusion of uniformly distributed internal heat sources. Accordingly, the nondimensional mass, momentum and energy conservation laws governing the convective flow take the form

$$\nabla \cdot \mathbf{v} = 0, \quad (1)$$

$$\nabla \cdot (2\eta(z)\dot{\epsilon}) - \nabla P = Ra_B \Delta T, \quad (2)$$

and

$$\frac{\partial T}{\partial t} = \nabla^2 T - \mathbf{v} \cdot \nabla T + \frac{Ra_H}{Ra_B}, \quad (3)$$

respectively. The nondimensional quantities in the above equations are: \mathbf{v} , velocity; $\eta(z)$, depth-dependent dynamic viscosity; $\dot{\epsilon}$, the strain rate tensor; P , pressure; T , temperature; and t , time. The independent model parameters associated with the

internal and basal heating in the systems are the internal heating and Bénard Rayleigh numbers:

$$Ra_H = \frac{\rho g \alpha \varepsilon d^5}{\kappa k \eta_o}, \quad (4)$$

and

$$Ra_B = \frac{\rho g \alpha \Delta T d^3}{\kappa \eta_o}, \quad (5)$$

respectively, where g is gravitational acceleration; α is thermal expansivity; ΔT , is the superadiabatic temperature difference between the top and bottom boundaries of the system; d , is the depth of the convecting layer; ρ is a reference density for the system; k , is the thermal conductivity; κ , is thermal diffusivity and η_o , is a reference dynamic viscosity. ε is the rate of internal heat generation per unit volume. The nondimensional internal heating rate is specified by the ratio $H = Ra_H/Ra_B$.

[8] The depth of our models scales to the thickness of the mantle. Thus all calculations feature isothermal top and bottom boundary conditions and a free-slip basal boundary condition. We examine models with both reflecting and periodic (wrap around) sidewalls. The convection code has been benchmarked for a variety of problems that do not include plates and shows excellent agreement with the results obtained from other numerical methods in those cases [e.g., Travis *et al.*, 1991; Busse *et al.*, 1993]. We use a parallelized version of MC3D and provide details on calculation resolution and requirements in the discussion of our results.

[9] Our calculations incorporate viscous finite thickness plates [e.g., Lowman *et al.*, 2003] and specified plate geometries. In this study, we initially prescribe steady plate velocities as well as fixed plate geometries in calculations featuring kinematic plate modeling [e.g., Lux *et al.*, 1979; van Keken and Gable, 1995; Jellinek *et al.*, 2003]. Subsequently, we explore convection in models that incorporate dynamically evolving plate velocities by implementing time-dependent boundary conditions that satisfy the requirement that the net force applied to each plate at all times is zero (that is, we balance the body forces driving the plate and the viscous resistance due to the plate motion). The force-balance method for modeling evolving plate velocities was described previously by Gable *et al.* [1991] and has been compared with material plate generation methods and the agreement between the methods was found to be excellent

Table 1. Physical Parameters for Mantle Convection Models

| Parameter | Value Employed in This Study |
|---------------|---|
| g | 10 ms^{-2} |
| d | 2900 km |
| η_0 | $9.26 \times 10^{20} \text{ Pa} \cdot \text{s}$ |
| α | $1.4 \times 10^{-5} \text{ K}^{-1}$ |
| ΔT | 2900 K |
| ρ | $4.7 \times 10^3 \text{ kgm}^{-3}$ |
| κ | $10^{-6} \text{ m}^2 \text{ s}^{-1}$ |
| k | $4.3 \text{ W}/(\text{m} \cdot \text{K})$ |
| ε | $2.22 \times 10^{-8} \text{ Wm}^{-3}$ |

for steady [King *et al.*, 1992] and time-dependent solutions [Koglin *et al.*, 2005].

[10] The subduction of cold sheet-like downwellings (slabs) is included in our calculations explicitly. Mass conservation results in the cooled upper thermal boundary layer material carried in the mechanical plates being forced into the mantle along convergent plate boundaries. Typically this results in the appearance of an anomalously cold sheet-like feature with the thermal signature of a descending slab. However, the omission of temperature-dependent viscosity in our calculations means that the cool, upper thermal boundary layer material (plate) that descends into the mantle at convergent plate boundaries does not have the strength of a slab. (The viscosity of the model is depth-dependent only.)

3. Results

[11] In all of the calculations presented here we specify a uniform internal heating rate with $H = 15$. This heating rate is based on the assumption that the rate of internal heating in the mantle is $4.7 \times 10^{-12} \text{ W kg}^{-1}$, roughly the heating rate estimated for the bulk silicate Earth derived from a chondritic starting condition [Stacey, 1992]. With this internal heating rate the ratio of the basal to the surface heat flux in our calculations is between 0.4 and 0.6, these values are in the range of values cited as characterizing the ratio of the mean core-mantle boundary heat flux to the mean surface heat flux excluding crustal sources [e.g., Buffett, 2003].

[12] The Bénard-Rayleigh number specified in all of our calculations is 5×10^7 and is determined by the values we adopt for the parameters given in Table 1. We specify the superadiabatic temperature gradient and mean mantle conductivities estimated

by Hofmeister [1999]. We specify a depth-dependent viscosity that begins to rapidly increase at 660 km depth and attains approximately ninety percent of its maximum value at a depth of 1660 km, after which the rate of increase becomes much more gradual. This stratified viscosity matches the general trend derived from joint inversions of post-glacial sea level histories and long-wavelength (up to spherical harmonic degree 8) convectively supported free air gravity harmonics [e.g., Forte and Mitrovica, 1996]. This viscosity profile was used previously in convection modeling studies by Pysklywec and Mitrovica [1997]. (These authors also present a plot of the viscosity depth dependence.) In total the viscosity features a factor of 36 increase with depth from the upper mantle to the deep lower mantle [e.g., Forte and Mitrovica, 1996]. (A variety of more complex viscosity models have cited similar ratios of lower mantle to upper mantle viscosity in two layer averaging calculations [e.g., Forte and Mitrovica, 2001].) The depth-variation of the viscosity is consistent with inferences based entirely on long-wavelength geoid anomalies [e.g., Hager, 1994; Richards and Hager, 1984; Ricard *et al.*, 1984; Forte and Peltier, 1987; King and Masters, 1992] and independent constraints on viscosity associated with observed long-term rates of polar wander [Sabadini and Yuen, 1989; Spada *et al.*, 1992]. A high viscosity layer at the top of the system acts as a first-order approximation for the stiffness associated with the Earth's cold oceanic lithosphere. This layer has a constant thickness of $0.037d$ (107.4 km) and is 1000 times more viscous than the reference viscosity employed in the determination of the Rayleigh numbers quoted in the remainder of this paper (see Table 1). The nondimensional viscosity at the base of the plates is $1.08 (10^{21} \text{ Pa} \cdot \text{s})$. Rayleigh numbers based on the highest viscosity in our stratified viscosity models are a factor of 36 smaller than that quoted above. With the choice of parameters stated in Table 1 the thermal diffusion time is approximately 266 Gyr. At all depths the mantle viscosity that we specify is necessarily high compared to estimated mantle values (by a factor of approximately 2 [Forte and Mitrovica, 1996, 2001; Mitrovica and Forte, 2004] due to computational constraints.

[13] To obtain an initial condition for each 3D model, we first obtain a solution to a two-dimensional problem with identical mantle parameters and an aspect ratio corresponding to the x dimension of the 3D calculation. The 2D (x - z dimensional) calculations include two-equal width

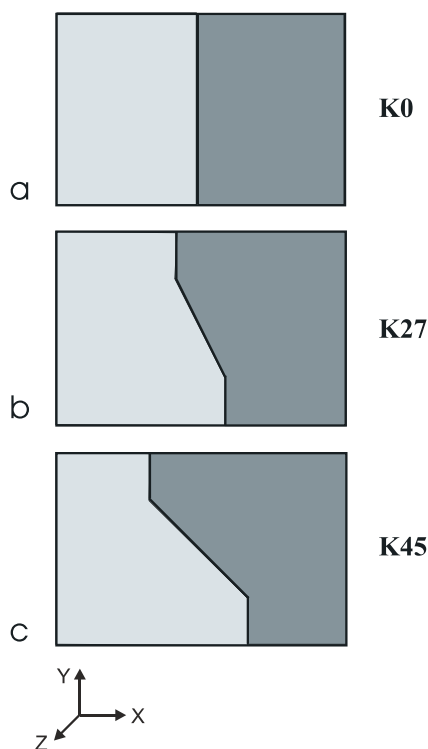


Figure 1. Plate geometries employed in the kinematic models. In each case the dark and lightly shaded plates are congruent. The central plate boundaries are convergent, and the plate boundaries at $x = 0.0$ and $x = 3.0$ (i.e., the vertical walls of the solution domain) are divergent. The sidewalls of the calculations are reflecting.

plates (specified by a 1D geometry in the x direction) and are integrated forward in time until they exhibit a statistically steady mean temperature, (i.e., a temperature time series that is showing no long term heating or cooling trends). To obtain the 3D solutions, we then project the 2D solution in the y direction and add random perturbations (i.e., we add perturbations to the temperature field of up to $0.01\Delta T$) and a 2D (x - y dimensional) plate geometry. We integrate the 3-D calculations for several mantle overturns before analyzing the results presented here.

3.1. Kinematic Plate Models

[14] We first consider a set of three calculations with specified, fixed, plate geometries and prescribed constant plate velocities. Each solution is obtained in a $3 \times 2 \times 1$ geometry (where the dimensions correspond to the x , y , and z coordinates, respectively). A reflecting side-wall boundary condition is specified. Solutions are obtained

using 32 processors and a numerical grid with $486 \times 324 \times 162$ elements.

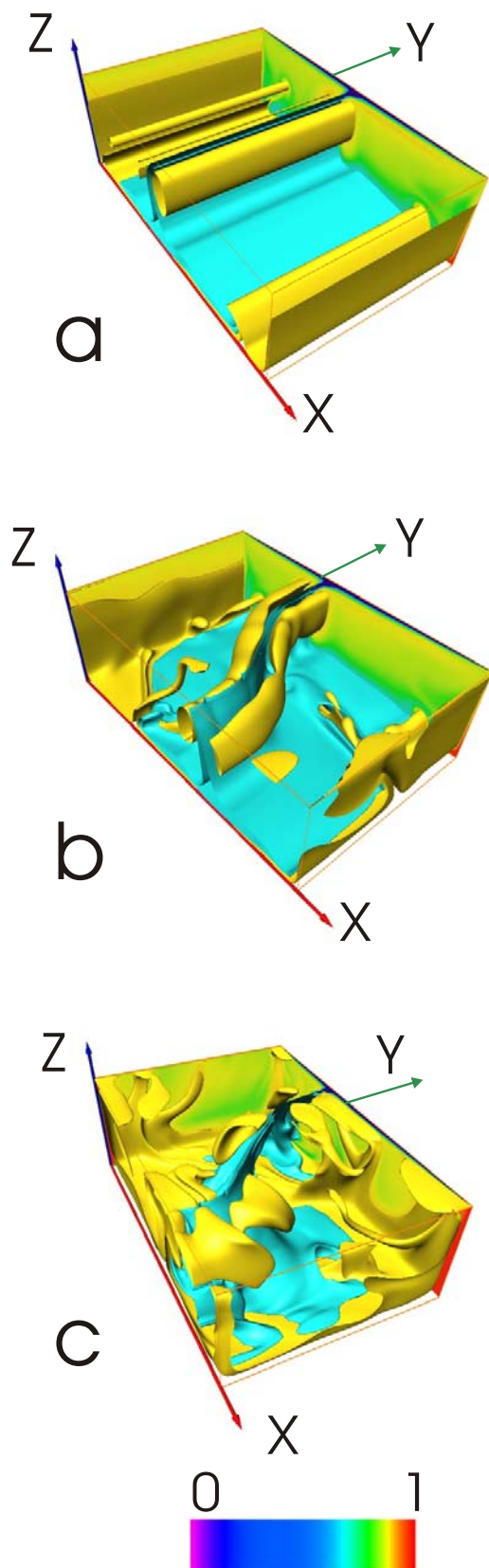
[15] Figure 1 shows the plate geometry specified in the three calculations. We refer to the snapshots from these time-dependent solutions as Models K0, K27 and K45. Each solution incorporates two plates and divergent plate boundaries at $x = 0.0$ and $x = 3.0$. Model K0 features a convergent plate boundary at $x = 1.5$. Model K27 includes a convergent plate boundary composed of three straight line segments, as shown in Figure 1b. (Note that extending the middle of the three segments produces an acute angle of 27.5° with each of the segments parallel to the y axis.) Model K45 also includes a convergent plate boundary composed of three straight line segments (in this case, extending the middle segment produces acute angles of 45° with the other segments).

[16] The vigor of the flow driven by the imposition of the surface motion is measured by the Peclet number, a nondimensional parameter defined by:

$$Pe = \frac{U_o d}{\kappa}. \quad (6)$$

Pe is the ratio of the timescale for thermal diffusion, κ , to the timescale for advection across the system depth, d , for flow driven at the surface velocity U_o . Accordingly, the Peclet number in these calculations gives the nondimensionalized surface velocity [e.g., Lux et al., 1979]. In each of the three calculations we specify that $Pe = 1839$, implying dimensionalized plate velocities of 2 cm/yr assuming a mantle depth of 2900 km and a whole mantle thermal diffusivity of $10^{-6} \text{ m}^2/\text{s}$. The plates move parallel to the x axis of the specified coordinate system. The combined plate velocities give a rate of plate convergence of 4 cm/yr.

[17] In Figure 2 we show snapshots of the temperature fields from Models K0, K27 and K45. The isosurfaces we plot are 15% colder (blue) and 15% hotter (yellow) than the mean temperature of the field. The top 100 km of the temperature fields have been removed in order to view the interior of the solution domain. Each model features a sheet-like downwelling plunging into the mantle along the length of the convergent boundary. These sheet-like features thicken as they descend as the velocity of the vertical flow decreases due to the increase in mantle viscosity with depth. Also prominent in these calculations are long, horizontally oriented, tube-like rolls of anomalously warm material created from the entrainment of heat



trapped below the plates by plate motion toward the convergent boundary. The presence of these features has been described in previous studies [e.g., Lowman *et al.*, 2001; Koglin *et al.*, 2005].

[18] Figure 2a shows a snapshot of the temperature field from Model K0 and indicates that in these highly time-dependent solutions the imposition of a boundary condition that is symmetric about $x = 1.5$ does not result in a symmetric flow around $x = 1.5$. In fact, the dip-angle of the downwelling cold sheet varies as this calculation evolves so that the downwelling shifts from dipping in the negative x direction to the positive x direction. Similarly, the temperatures of the warm rolls oscillate so that the hotter side of the downwelling alternates. For example, in the figure, the hot roll that appears farthest from the viewer's position is smaller and cooler than the nearer roll. However, at an earlier time (as will again be the case at a later time) the near roll appears smaller and cooler. Despite the time dependence of the solution, the thermal gradients in the y direction in this calculation are tiny and the flow is essentially two-dimensional.

[19] Figure 2b shows a snapshot of the temperature field from Model K27 and reveals that, combined with the inherent time dependence of these systems, the introduction of plate geometry variability in the y direction has resulted in thermal gradients in the downwelling cold sheets (indicated by ripples in the isosurface) and accompanying hot rolls parallel to the convergent plate boundary. This is due to the influence of the plume-like upwellings that have appeared in the solution. The change in the boundary condition thus excites three-dimensional flow throughout the mantle system. The differing sizes of the convection cells on each side of the consumed plate material results in a variation in the dipping angle of the cold downwelling along the convergent plate boundary with the cold downwelling angled toward the plate that is smallest in 2D slices parallel to the x axis.

[20] Figure 2c shows a snapshot of the temperature field from Model K45 and illustrates that increas-

Figure 2. Temperature field snapshots of Models (a) K0, (b) K27, and (c) K45. The solution domain is $3 \times 2 \times 1$, and the model sidewalls are reflecting. The yellow and blue isosurfaces are 15% warmer and cooler, respectively, than the mean temperature of the calculations, 0.64 (the mean in all three calculations). The coordinate axes indicate the x (red), y (green), and z (blue) directions corresponding to the axes shown in Figure 1.

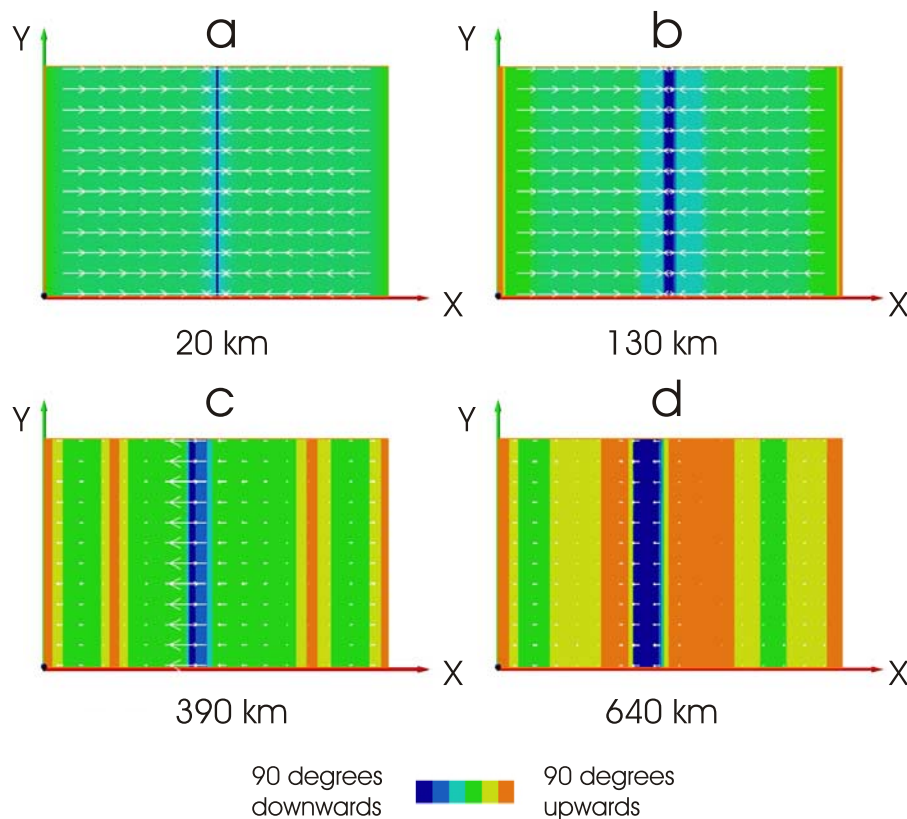


Figure 3. Horizontal flow velocity and flow velocity angle in Model K0 at depths of (a) 20 km, (b) 130 km, (c) 390 km, and (d) 640 km. Flow velocity angle is divided into six ranges: navy and orange show regions with down dipping and rising flow, respectively, at angles that are more than 60° from horizontal; blue and yellow show regions with down dipping and rising flow, respectively, that are more than 30° and less than 60° from horizontal; and cyan and green show regions with down dipping and upward flow, respectively, that is within 30° of horizontal. The arrows indicating the direction and magnitude of the flow velocity in the horizontal plane have a length that is linearly proportional to the flow velocity magnitude. The length of the arrows in Figure 3a approximately indicates the plate velocity of 2 cm/yr. The coordinate axes indicate the x (red), y (green), and z (blue) directions corresponding to the axes shown in Figure 1.

ing the length of the convergent plate boundary and the amount of strike-slip motion in the boundary condition velocity field (toroidal power) has resulted in a flow characterized by pronounced downwelling dip angles, numerous three-dimensional upwellings, and isolated pockets of anomalously hot material juxtaposed alongside the downwellings. Variation of the plate geometry in the y direction has resulted in a flow that shows considerable variation in the y direction even though the plate motion is still parallel to the x axis. The appearance of hot pockets of material spaced-out alongside the downwelling flow, rather than a uniform hot tube, is explained by the arrival of plate-motion-entrained, detached, hot plume heads at different locations along the downwelling sheet. Consequently, angling the strike of the plate boundary

with respect to the plate motion vectors has resulted in a transition to thoroughly developed 3D flow and significant temperature gradients in regions parallel to, and enveloping, the downwelling flow. The ability of the plate boundaries to generate 3D flow deep in the system is a result of the advection of 3D thermal features generated along the plate boundary, to locations deep in the system where they influence heat flux across the lower thermal boundary layer.

[21] The total velocity field in our calculations can be decomposed into vertical and horizontal components. Accordingly, we write the total velocity field as $\vec{V}_t = \vec{V}_h + \vec{V}_z$, where \vec{V}_h is the horizontal and \vec{V}_z is the vertical component of the total nondimensional velocity field \vec{V}_t . Regions domi-

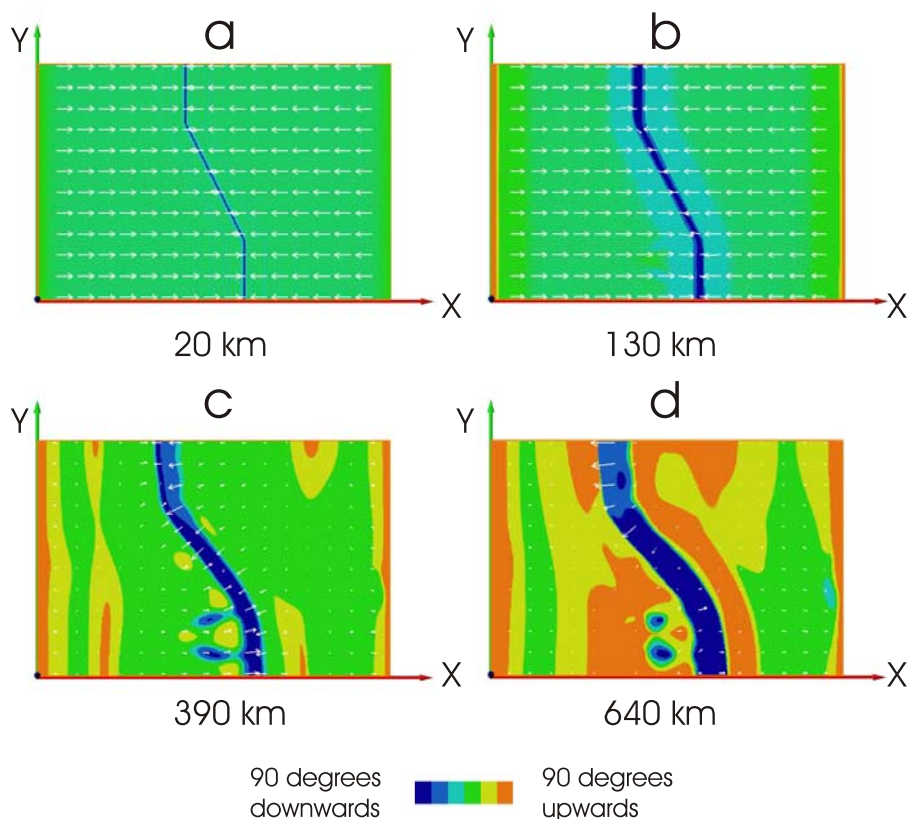


Figure 4. Horizontal flow velocity and flow velocity angle in Model K27 at depths of (a) 20 km, (b) 130 km, (c) 390 km, and (d) 640 km. Flow velocity angle is indicated in color as in Figure 3. Arrows indicate horizontal velocity as in Figure 3. The length of the arrows in Figure 4a approximately indicates the plate velocity of 2 cm/yr. The coordinate axes indicate the x (red), y (green), and z (blue) directions corresponding to the axes shown in Figure 1.

nated by vertical flow can be separated from regions characterized by significant horizontal flow by plotting the angle $\theta = \arctan(|\vec{V}_z|/|\vec{V}_h|$.

[22] In Figure 3 we plot the angle θ at four different depths in Model K0. The value of θ is indicated with a color scale showing the angle of the flow vector relative to horizontal in six different 30° ranges. For example, navy indicates downward flow dipping at an angle between 60° and 90° from horizontal while orange indicates upward flow rising at an angle between 60° and 90° from horizontal. Also shown in Figure 3 with the use of white arrows is the horizontal flow direction and magnitude. The arrows indicate the horizontal flow direction and magnitude at the location where their tail terminates. If we refer to arrows as starting in these locations then arrows starting in a cyan or green region indicate velocity where the flow direction is within 30° of the horizontal plane. Arrows starting in yellow or blue regions indicate intermediate upward and downward flow, respec-

tively. Arrows starting in green or cyan regions are therefore the most indicative of actual flow direction. Arrows starting in other regions will have significant vertical flow components.

[23] Figures 3a, 3b, 3c, and 3d show θ and the horizontal flow vectors in Model K0 at depths of 20 km, 130 km, 390 km and 640 km, respectively. The arrow scale is the same in all four figures. The figure shows that very uniform, predominantly horizontal, flow exists just below the plates at a depth of 130 km and that flow velocity at this depth is comparable to the flow in the viscous plate (Figure 3a). However, deeper in the upper mantle, horizontal flow velocities are significantly reduced everywhere other than in the downwelling region. Upward flow exists in regions parallel to (and approximately mid-way between) the plate boundaries in each convection cell but it is very weak. At the base of the upper mantle (Figure 3d) horizontal flow is weak and wide regions containing weak

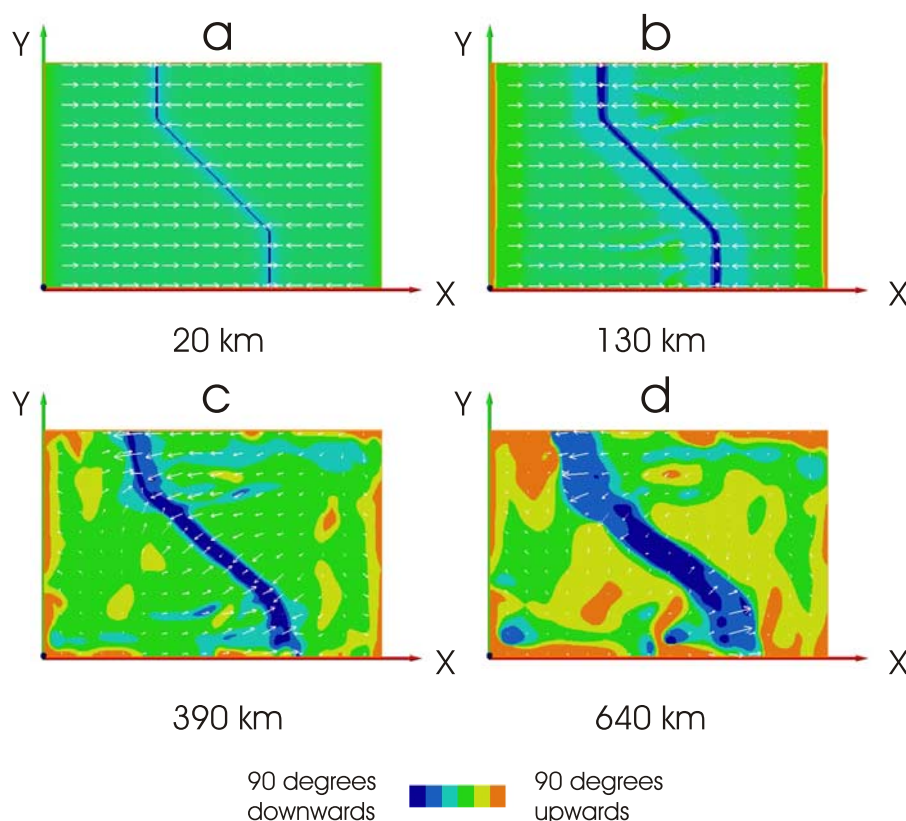


Figure 5. Horizontal flow velocity and flow velocity angle in Model K45 at depths of (a) 20 km, (b) 130 km, (c) 390 km, and (d) 640 km. Flow velocity angle is indicated in color as in Figure 3. Arrows indicate horizontal velocity as in Figure 3. The length of the arrows in Figure 5a approximately indicates the plate velocity of 2 cm/yr. The coordinate axes indicate the x (red), y (green), and z (blue) directions corresponding to the axes shown in Figure 1.

upward flow lie parallel to the central region of downwelling flow. The broad orange regions in the figure are associated with upwelling flow in the warm, tube-like, rolls that lie adjacent to the downwelling flow in the model.

[24] In Figure 4 we show flow angle and horizontal flow for Model K27 at the same depths that were examined in Figure 3. The arrow scale is the same in all four panels of the figure, although it is different from Figure 3. Flow at 130 km is essentially aligned in the direction of the plate movement and has comparable magnitude to the plate velocity. Consequently, a nonzero component of the horizontal flow vector exists parallel to the convergent plate boundary in regions where the plate convergence is oblique to the plate boundary. At 390 km depth the horizontal flow vectors have rotated so that flow is roughly orthogonal to the cold downwelling sheet in the calculation along its entire length. The influence of the motion of the

plate is minimal compared to the driving force associated with the sinking material from the cold consumed plates. As in Model K0, horizontal flow is minor at a depth of 640 km and a broad diffusive upwelling region envelops the downwelling sheet.

[25] In Figure 5 we show similar results for Model K45. Figure 5b shows similar behavior to previous models where plate motion dominates flow direction just below the plate. The increase in the length of the convergent plate boundary and the obliquity of the plate motion to the boundary produces strong horizontal shear (toroidal flow) in the solution. However, flow at a depth of 390 km is still dominated by the buoyancy distribution in the thermal field. That is, horizontal flow does not exhibit a significant component of plate boundary parallel flow like that driven by the plate motion. The shape of the downwelling sheet causes flow at this depth to rotate relative to the direction of the plate

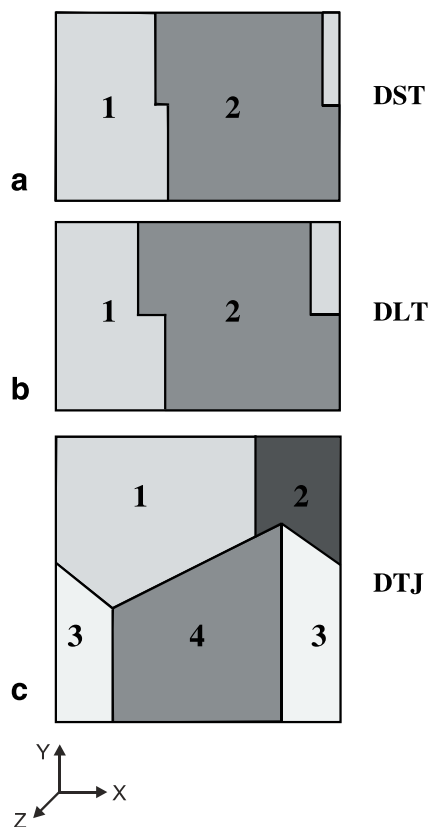


Figure 6. Plate geometries employed in the dynamic plate models. The solution domain sidewalls are periodic. Consequently, plates may be intersected by the bounds of the solution domain. For example, Plate 1 in Figures 6a and 6b and Plate 3 in Figure 6c are each shown to wrap around the solution domain.

motion so that motion is predominantly directed toward the nearest section of cold downwelling.

[26] The results of these experiments show that the influence of the plate-driven toroidal flow does not penetrate very far below the viscous plates. Flow direction is dominated by the temperature field. Flow in the mid-upper mantle is almost perpendicular to the strike of the downwelling cold sheet at most locations.

3.2. Dynamic Plate Models

[27] We now consider a suite of calculations performed with specified plate geometries but evolving plate velocities. Each of the calculations discussed is highly time-dependent and we examine the flow solutions at arbitrary instants in time. All solutions are periodic (wrap around) in the x and y directions. Figure 6 shows the prescribed plate geometry in each of the calculations we have investigated and Figure 7 shows a snapshot of the

temperature field from two of the calculations. In the discussion that follows we refer to these solutions as Model DST, a dynamic plate model featuring long straight convergent and divergent plate boundaries that each incorporate a pair of short transform fault-like sections and Model DLT, a similar model featuring longer transform fault sections.

[28] Figure 7a (Model DST) shows that flow in Model DST is dominated by a pair of convection

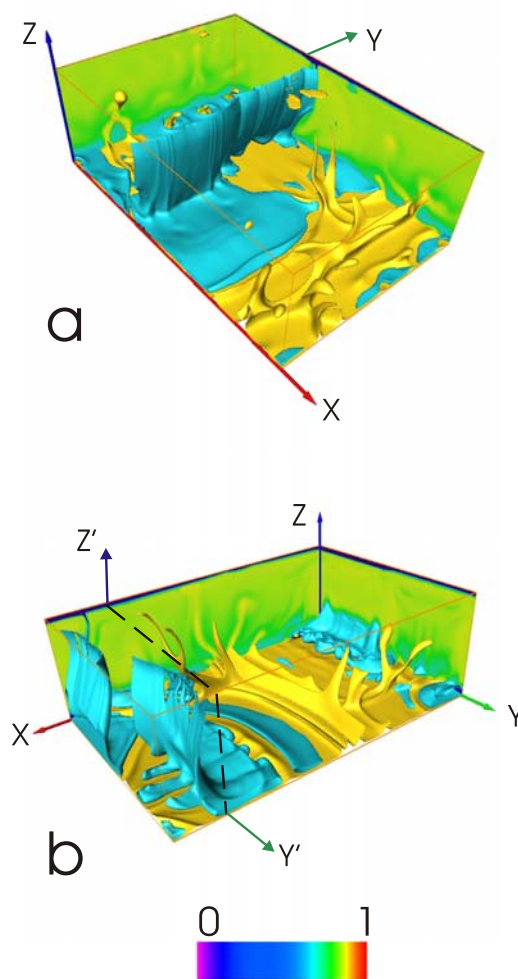


Figure 7. Temperature field snapshots of Models (a) DST and (b) DLT. The solution domain is $3 \times 2 \times 1$, and the model sidewalls are periodic. The yellow and blue isosurfaces are 15% warmer and cooler, respectively, than the mean temperature of the calculations, 0.73 (the mean in both models). The coordinate axes indicate the x (red), y (green), and z (blue) directions corresponding to the axes shown in Figure 6. The x' and z' axes (and the box created by the dashed lines) shown in Figure 7b are relevant to Figures 10 and 11.

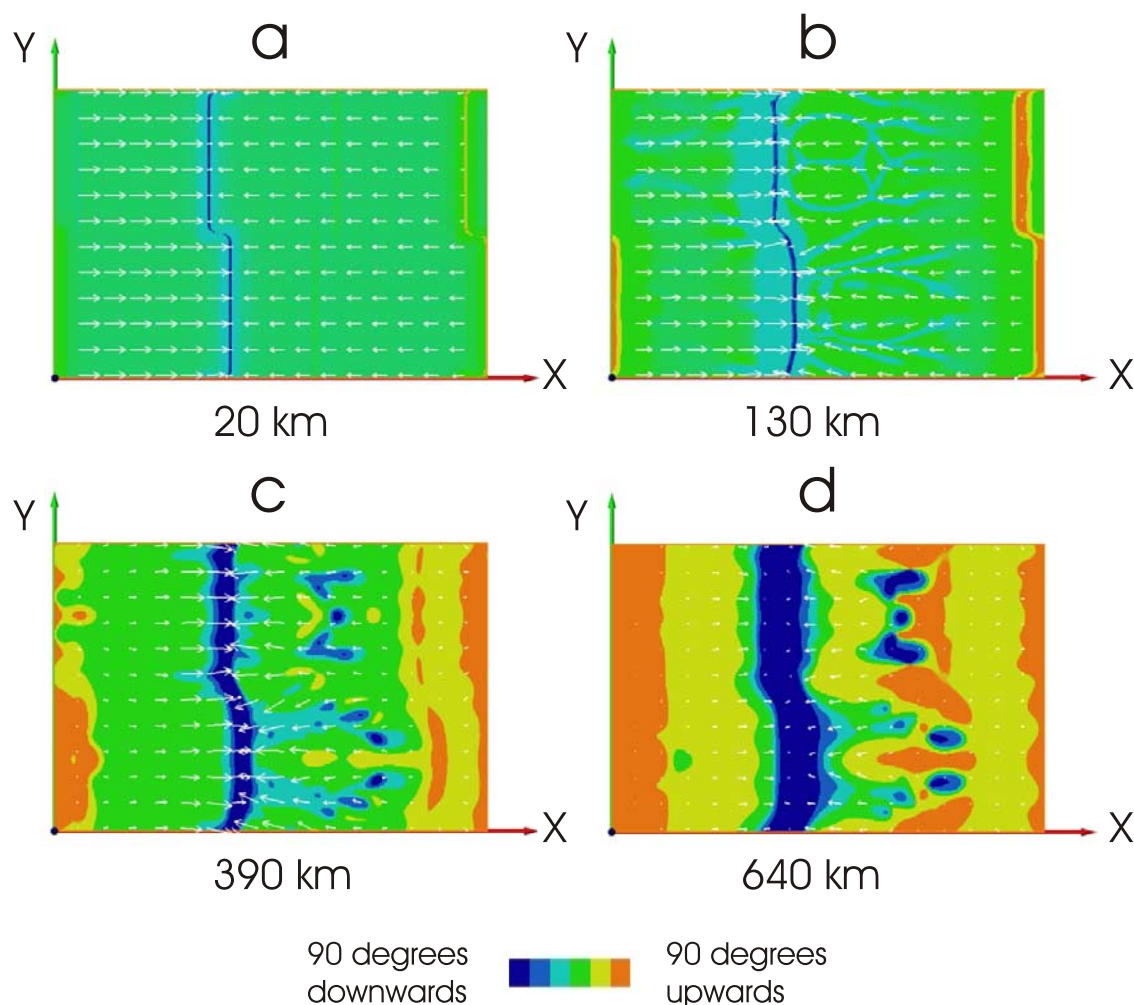


Figure 8. Horizontal flow velocity and flow velocity angle in Model DST at depths of (a) 20 km, (b) 130 km, (c) 390 km, and (d) 640 km. The color convention indicates flow angle as in Figures 3, 4, and 5. The arrows indicating the direction and magnitude of the component of flow velocity in the horizontal plane have a length that is linearly proportional to the flow velocity magnitude. The length of the arrows in Figure 8a indicates the approximate plate velocity. The coordinate axes indicate the x (red), y (green), and z (blue) directions corresponding to the axes shown in Figure 6.

cells with roll-like geometry, however, in contrast to Model K0, the variation in the plate geometry in the y direction has allowed for three-dimensional features such as upwelling plumes to develop. The three-dimensional flow in the calculation is also excited by the time-dependent velocity that allows linear boundary layer instabilities to develop below the viscous plate. These downwelling features result from the shearing of Rayleigh-Taylor instabilities by the plate motion which results in the alignment of a secondary mode of small-scale convection rolls with axes parallel to the direction of plate motion [e.g., Richter, 1973; Richter and Parsons, 1975; van Hunen et al., 2003; Korenaga and Jordan, 2004]. The large downwellings below

the convergent plate boundaries are sheet-like but clearly vary in the y direction. Linear, vertical, ridges and grooves are apparent on the cold downwelling isosurface and result from the subduction of the linear downwelling features associated with the small-scale convection that aligns with the direction of plate motion prior to consumption at the convergent plate boundary.

[29] Figure 7b (Model DLT) shows that increasing the length of the transform fault results in two distinct, detached, sections of downwelling material. Overall, the flow is still dominated by a flow pattern characterized by a pair of large-scale convective rolls. Upwellings evolve from sheet-like

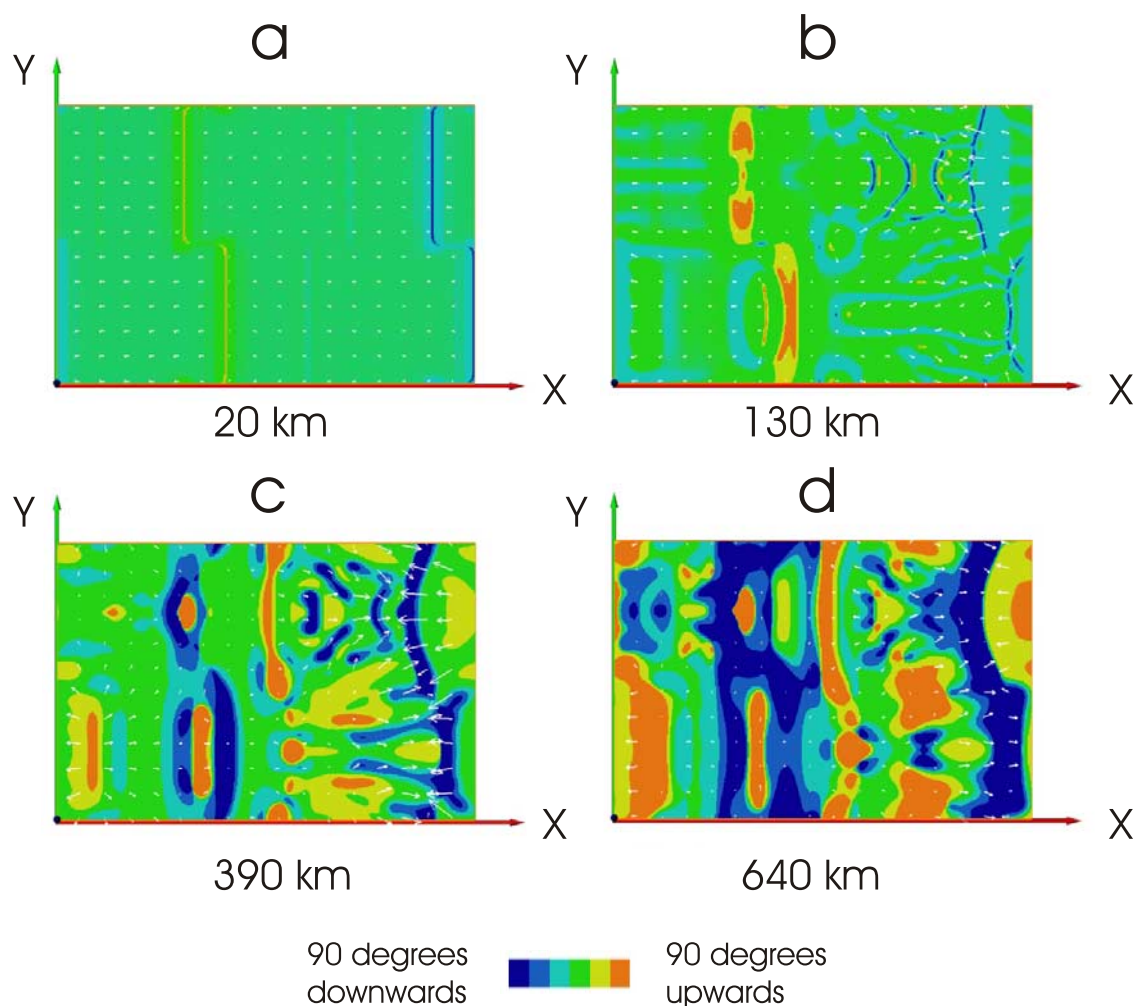


Figure 9. Horizontal flow velocity and flow velocity angle in Model DLT at depths of (a) 20 km, (b) 130 km, (c) 390 km, and (d) 640 km. The color convention indicates flow angle as in Figures 3, 4, and 5. The arrows indicating the direction and magnitude of the component of flow velocity in the horizontal plane have a length that is linearly proportional to the flow velocity magnitude. The length of the arrows in Figure 9a indicates the plate velocity. The coordinate axes indicate the x (red), y (green), and z (blue) directions corresponding to the axes shown in Figure 6.

features in the lowest part of the mantle into plume-like features in the mid- and upper mantle. Small-scale upper mantle convection rolls aligned with the direction of plate motion are again present.

[30] Figure 7b includes a second set of axes marked $x'-y'$. In later figures the origin created by the intersection of these axes with the x axis is used as a reference point in a cut-out region of the full solution domain. The cut-out is used to focus on the detail around the downwelling sheets.

[31] Although they are not as evident as in the results from the kinematic plate experiments, anomalously hot parcels of material periodically

build and envelop the sheet-like downwellings in each of the dynamic plate experiments shown in Figure 7. In response to the stresses these warm regions exert on the base of the plates, plate velocities periodically slow down or reverse direction altogether [e.g., Lowman *et al.*, 2001; Koglin *et al.*, 2005].

[32] Figure 8 shows the angle of the velocity vectors and the magnitude and direction of the horizontal components of the velocity in Model DST at depths of 20 km, 130 km, 390 km and 640 km. The same velocity scale is used for the arrows in each case. The results differ only slightly

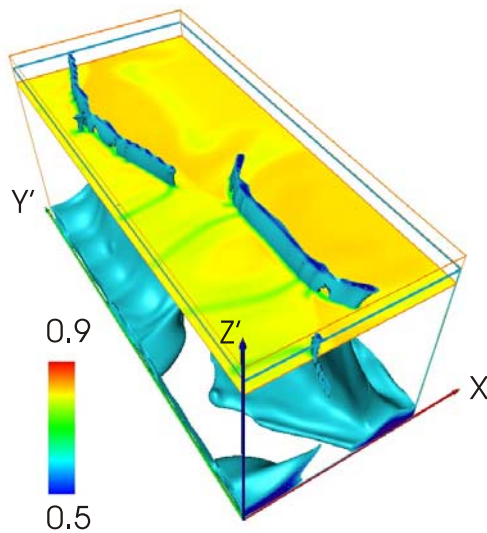


Figure 10. Temperature field detail in Model DLT showing a horizontal slice through the solution domain and the two sheet-like downwellings in Figure 7b. The horizontal slice through the solution domain is at a depth of 390 km, the same depth as the slice shown in Figure 9c. The x (red) axis is aligned with the x axis in Figure 7b, but the origin of the coordinate system has been translated in the x direction. The x' and y' axes shown here were shown in Figure 7b for reference. The section of the field plotted has dimensions of $0.86 \times 2.0 \times 1.0$.

from those observed in the kinematic plate experiments. Specifically, the addition of the small-scale convection at the base of the plates causes deflection of the flow direction at the base of the plates (Figure 8b) so that the horizontal flow is not aligned with the plate direction at all locations. At a depth of 390 km, horizontal flow is roughly perpendicular to the contours around the steepest dipping vertical flow (i.e., the cold downwelling).

[33] Figure 9 is analogous to Figure 8 but shows results from Model DLT. The arrow scale is again constant in all four figures. However, because the randomly chosen snapshot presented here occurs at a time when the time-dependent plate velocity is lower than average, the arrows shown in Figure 9a are shorter than the near surface velocity arrows in previous figures. The length of the transform fault section between the distinct downwelling sheets in this calculation means that, in contrast to previous calculations, Model DLT includes downwellings that have a finite extent in the y direction. Moreover, despite the linear plate boundaries, horizontal slices show the downwelling sheets become curved

as they descend into the upper mantle, adding to the three-dimensionality of the flow. The complexity of the 3D flow at the edges of the downwelling sheets is evident in Figures 9b and 9c. Specifically, Figure 9c shows that flow in between the sinking slab segments is mainly horizontal (arrows start in green and cyan regions), relatively fast, and is moving almost parallel to the contours outlining the fastest descending (blue and navy) part of the flow associated with the slabs. Arrows placed between the offset slabs indicate that flow is neither toward the downwelling slab nor in the direction taken by the plate above. Moreover, the roughly horizontal flow squeezing between the offset ends of the descending slabs has a rising component (it is in a green region). The rising component of the flow indicates that the material squeezing between the slabs is buoyant.

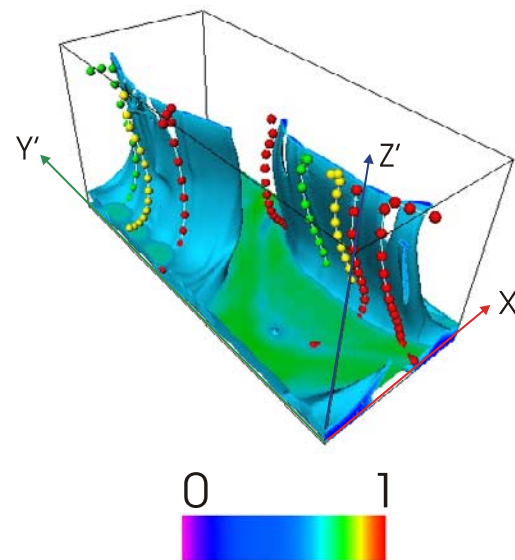


Figure 11. Flow streamlines and isosurfaces for a temperature of 0.6205 in Model DLT. The x (red) axis is aligned with the x axis in Figure 7b, but the origin of the coordinate system has been translated in the x direction. The x' and y' axes shown here were shown in Figure 7b. The two sheet-like downwellings shown in Figure 10 are depicted for reference. The downwelling isosurfaces are only shown below a depth of 320 km. The streamline segments shown are indicated by white lines and descend from a depth of 320 km. Adjacent colored spheres divide the streamlines into segments corresponding to distances that would be traveled along the streamline in a period of $5 \times 10^{-5} d^2/\kappa$. Different colors distinguish individual trajectories but have no physical meaning.

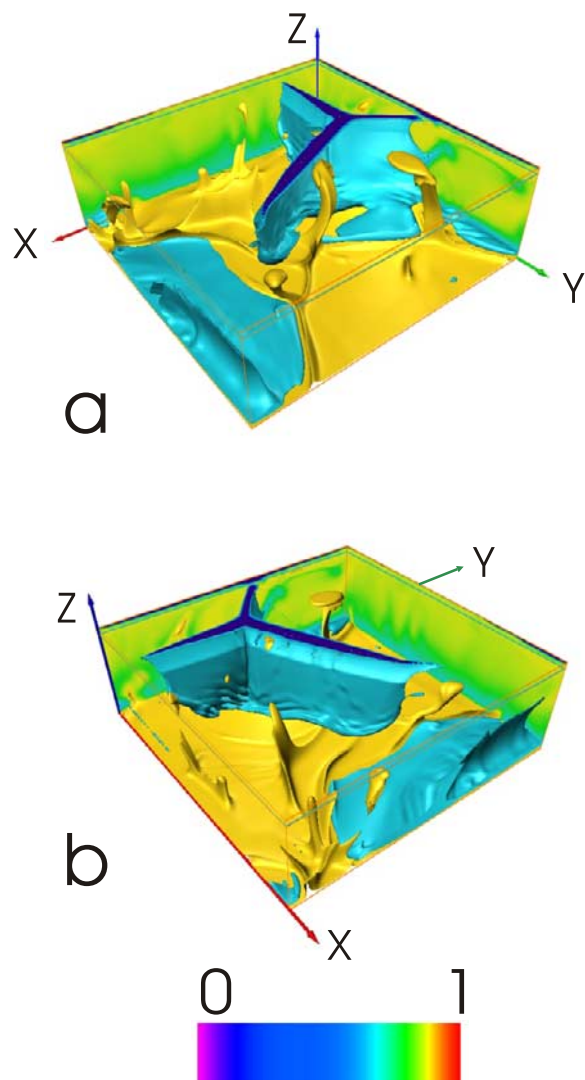


Figure 12. Two views of the temperature field of Model DTJ. The solution domain is $3 \times 3 \times 1$ (resolved by a grid incorporating $325 \times 325 \times 129$ computing nodes), and the model sidewalls are periodic. The yellow and blue isosurfaces are 15% warmer and cooler, respectively, than the mean temperature of the calculation, 0.75. The coordinate axes indicate the x (red), y (green), and z (blue) directions corresponding to the axes shown in Figure 6.

[34] Figure 10 shows a detailed section of the temperature field from Model DLT. The horizontal slice shown is at a depth of 390 km, the same depth as the slice in Figure 9c. The same cold isosurface included in Figure 7b is also shown. The axes shown in the figure indicate the positive x (red), y (green), and z (blue) directions but the origin of the system does not correspond to the origin in Figure 7b. The width of this section of the solution

is $0.86d$ (2494 km) in the x direction. This figure shows that material on one side of the downwelling slabs is warmer at a depth of 390 km than material on the other side of the descending slabs. The horizontal temperature gradient explains the observation that the flow in this region moves below the transform fault in a direction parallel to the strike of the downwelling sheet. The warm material is part of a hot pocket of material lying adjacent to the downwelling, it forms from heat trapped below the plates in the same way as the hot rolls of material observed in previous calculations like Models K0 and K27. The difference in temperature on each side of the downwelling sheets is most likely explained by the different sizes of the noncongruent plates in this calculation.

[35] In Figure 11 we plot eight streamlines as indicators of the direction of the flow motion in Model DLT. The streamlines are obtained for the velocity field that corresponds to the temperature field snapshot in Figure 10. We assume that for brief periods the streamlines approximate particle trajectories and the time-dependent velocity fields can therefore be treated as steady [e.g., *van Keken and Zhong, 1999*]. We use trilinear spatial interpolation of the velocity and a fourth-order Runge-Kutta scheme for the time integration.

[36] Spherical markers are plotted along the streamlines at intervals that produce segments corresponding to the distance that a particle traveling along the streamline would traverse in $5 \times 10^{-5} d^2 / \kappa$ (approximately 13.3 Myr; see Table 1). The different colors used for the markers have no physical meaning. Each streamline is calculated from a starting point at a depth of 320 km. The cold, blue, temperature field isosurface in the figure is only shown below this depth. A horizontal slice through the temperature field is shown at a depth of 2510 km. The streamlines show that, away from the downwelling edges, flow moves toward the downwelling sheet and then straight down. However, near the edge of the downwelling sheets, flow moves approximately horizontally and parallel to the downwelling for over 500 km, before descending (the right-most red path in the figure). The results from Model DLT indicate that, near the edges of the cold features, mid-upper mantle flow does not everywhere move directly toward the closest cold downwelling.

[37] Finally, we consider flow in a highly time-dependent calculation. In Figure 12 we present two views of a temperature field snapshot from Model DTJ. This calculation has the most time-dependent

plate velocities of the models examined and exhibits rapid changes in the direction of plate motion and plate velocities at regular intervals [e.g., *King et al.*, 2002]. A numbering convention was introduced for the four plates in this calculation in Figure 6 and is referred to in the text below. As in Figures 2 and 7, the isosurfaces correspond to temperatures 15% cooler (blue) and warmer (yellow) than the mean temperature of the system. At the instant shown, the flow features three young sections of sheet-like downwellings that meet at a triple junction. The downwelling sheets have penetrated to different depths in the lower mantle. The oldest section is the right-most section in Figure 12a. The youngest section is the sheet parallel to the (green) y axis.

[38] The boundary conditions and geometry of Model DTJ allow for a greater degree of freedom of both the plate motion and fluid motion than in the other cases examined. In contrast to a pair of plates that are limited to instilling a roll-like convection pattern in the convecting fluid by their opposing motion, the plate geometry in Model DTJ allows for an unlimited variety of flow patterns given the freedom for three plates to balance the motion of the fourth plate. The time dependence of this calculation was discussed previously by *King et al.* [2002]. The sequence we present as Model DTJ occurs at a time when a system of downwelling sheet-like features join at a triple junction. Simultaneously, the vestiges of an old terminated downwelling are descending into the lower mantle well away from the triple junction of convergent boundaries.

[39] Figure 13 shows the flow in Model DTJ at depths of 20 km, 140 km, 410 km and 630 km. The arrows in Figure 13a show the direction of the plate movement at the instant considered. Flow below the plates (Figure 13b) is almost identical to that in the plates, both in direction and in magnitude. Figure 13c shows that horizontal flow direction at a depth of 410 km can differ considerably from the flow direction of the plates. Flow near the youngest downwelling (parallel to the y axis) is actually parallel to the downwelling sheet over a distance of nearly 3000 km below Plate 4 (defined in Figure 6). Similarly, flow along the other downwelling sheet bounding Plate 4 exhibits regions where the flow appears to be parallel to the downwelling. In contrast, horizontal flow below Plates 1 and 3, which also border convergent boundaries, moves directly toward the downwelling sheets. At a depth of 630 km the flow is

predominantly vertical and horizontal flow no longer appears to move parallel to downwellings in any region. Low horizontal velocities are typical in the depth range 600–1000 km in our calculations. High velocity horizontal flow is generally confined to the upper mantle while a lower velocity return flow is dispersed through the deep mantle and increases toward the base of the system.

[40] In Figure 14 three views are shown of the temperature field from Model DTJ. Also included in the figure are five streamlines. Only that part of the cold surface laying below a depth of 405 km is shown. A horizontal slice through the temperature field at a depth of 2510 km is also drawn. The streamlines were calculated using the flow field corresponding to the timing of the temperature field snapshot. The streamlines are marked by red, green and yellow spheres placed at intervals that divide the streamlines into segments having lengths equal to the distance that a particle traveling along the streamline would traverse in a period of $2.5 \times 10^{-5} d^2/\kappa$ (about every 6.65 Myr). We note that flow below Plate 4 to the right of the convergent boundary between Plates 3 and 4 (see Figure 6 for definitions) is moving almost parallel to the adjacent, cold, downwelling sheet and continues to move horizontally and parallel to the downwelling over distances of thousands of kilometers. In order to check the consistency of the result and the dependence on starting position, we show streamlines with three different starting points in this region (red, yellow and green) and find the result is similar at all three of the locations examined. Flow at the other locations that we investigated in this solution generally moves straight toward the closest downwelling.

[41] Model DTJ is taken from a rapidly evolving sequence in a particularly time-dependent calculation. In order to determine whether the flow pattern indicated in Figure 14 is a short-lived anomaly we calculated a number of particle trajectories in the flow fields that evolve during the 26 Myr period following the snapshot shown in Figure 14. If the flow is maintained long enough it might result in the development of lattice-preferred orientation (LPO) that would produce a fast direction for seismic velocities oriented parallel to the strike of the downwelling slab-like feature described above.

[42] Figure 15 shows the 0.6205 temperature field isosurface at the end of the 26 Myr period just described and a curve segment (in red) corresponding to one of the particle trajectories calculated. As was the case in calculating model streamlines we

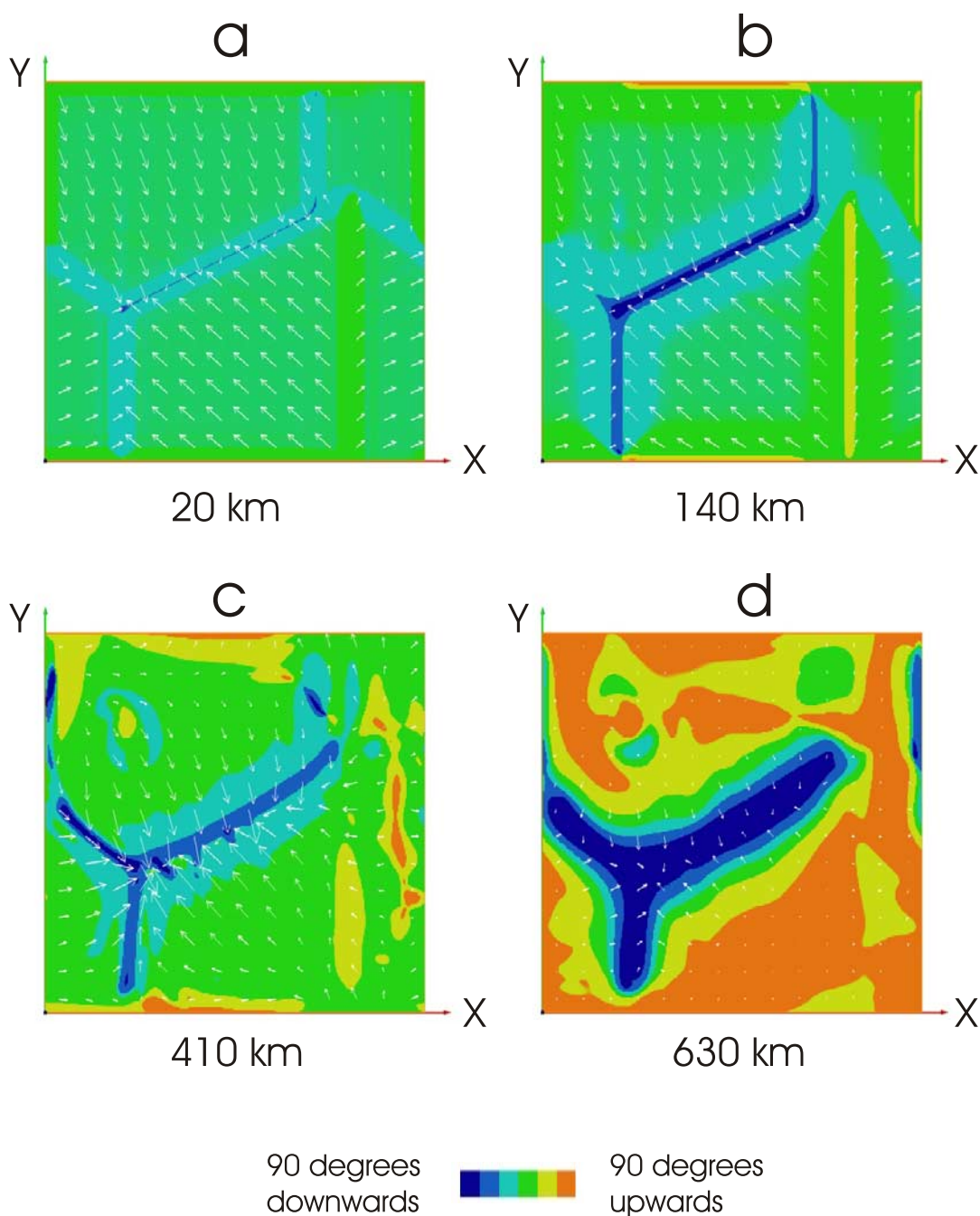


Figure 13. Horizontal flow velocity and flow velocity angle in Model DTJ at depths of (a) 20 km, (b) 140 km, (c) 410 km, and (d) 630 km. The color convention indicates flow angle as in Figures 3, 4, and 5. The arrows indicating the direction and magnitude of the flow velocity in the horizontal plane are proportional in length to the flow velocity magnitude. The length of the arrows in Figure 13a indicates the approximate plate velocity. The coordinate axes indicate the x (red), y (green), and z (blue) directions corresponding to the axes shown in Figure 6.

calculate trajectories using a fourth-order Runge-Kutta scheme with trilinear spatial interpolation. In order to determine whether the accumulated strain on a parcel of mantle material traveling along this trajectory would result in a deformation of the

mineral fabric consistent with the development of a fast direction for seismic velocities parallel to the slab, we have calculated the deformation of a 42 vertex polyhedron probe which can be placed in the model's velocity field. The probe is obtained by

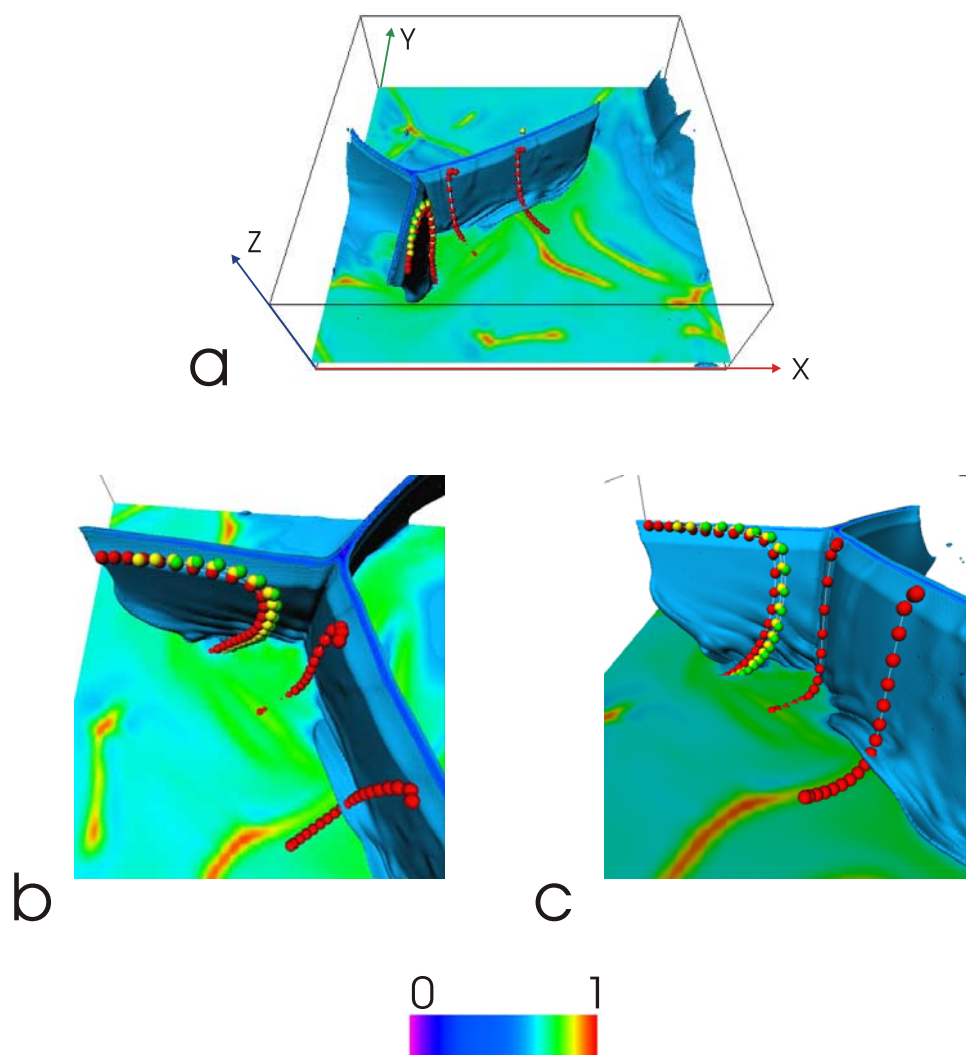


Figure 14. Flow streamlines and isosurfaces for a temperature of 0.6205 in Model DTJ. The bottom frames in the figure show different viewing angles of the same streamlines shown in the top frame. The downwelling isosurfaces are only shown below a depth of 405 km. Streamlines are indicated by white lines that are divided into sections by the placement of colored spherical markers. The intervals of separation of the spheres correspond to the distance that would be traveled along the streamline in a period of $2.5 \times 10^{-5} d^2/\kappa$. Each streamline descends from a depth of 405 km. Different colors distinguish individual streamlines but have no physical meaning.

adding a vertex at the midpoint of each edge of a regular icosahedron. (In the remainder of this paper we shall refer to the initial shape of the probe as icosahedral). The probe is therefore approximately spherical in shape at the time at which it is introduced into the calculation, however, it is free to deform subsequently. The probe does not interact with the flow; its vertices are passive markers that define an enclosed volume. The initial central point of the probe travels the trajectory shown in Figure 15. The deformation of the probe is deter-

mined by calculating the trajectories of each of the 42 vertices of the icosahedron. The flow is incompressible thus the volume of the probe is maintained.

[43] Figure 16 shows the before and after morphologies of the probe. Its initial maximum width is approximately 250 km. The figure shows four views of the probe revealing its relative before and after positions and the translation of selected vertices (marked with different colors). The coordinates on the black axes in the figures give the

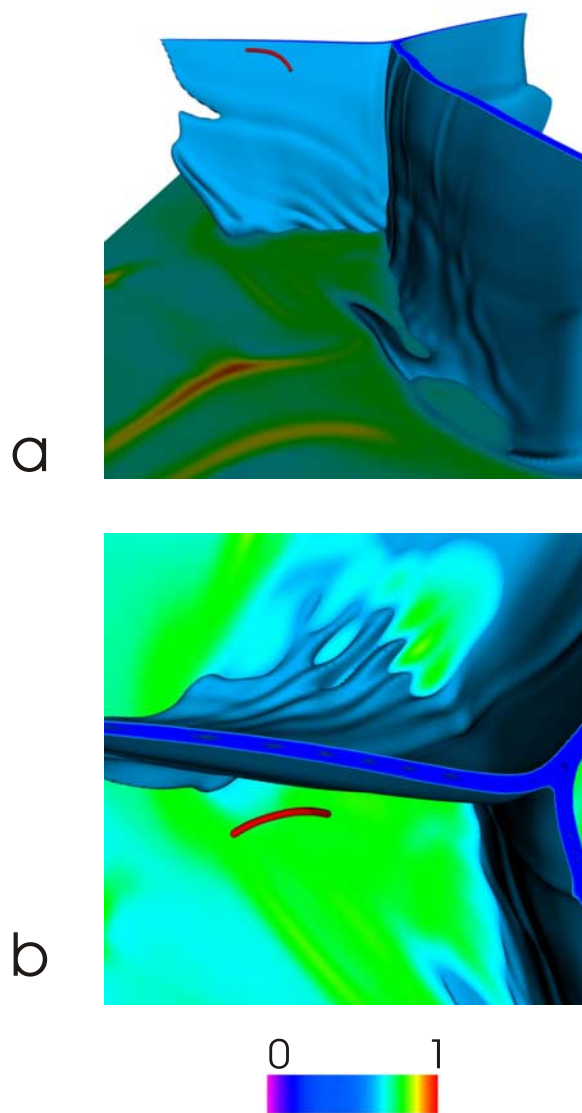


Figure 15. The trajectory (the section of red curve) taken by the initial central point of the icosahedral probe described in the text. Also shown for reference are the temperature field isosurface corresponding to a temperature of 0.6205 and a corresponding horizontal slice through the temperature field at a height of 405 km above the base of the system. The downwelling isosurfaces are only shown below a depth of 405 km. The temperature field depicted in this figure is from a snapshot corresponding to the final time used in the integration that determined the trajectory of the probe. The integration began at the time associated with the temperature field shown in Figures 12 and 14. Using the values given in Table 1, we calculate that the probe travels the trajectory shown over a period of approximately 26 Myr.

position of the probe in the $3 \times 3 \times 1$ solution domain relative to the origin indicated in Figure 12. The icosahedron is rotated and sheared as it travels adjacent to the slab, finally obtaining a somewhat flattened, broad, teardrop shape. The initial parcel of material is stretched in the y and z directions as its initial central point follows the path shown. From this deformation we infer that an LPO would develop that would yield a fast direction for seismic velocities parallel to the strike of the neighboring slab.

[44] The findings revealed in Figures 13–16 show that the freedom of movement in three-dimensional flows results in complex, difficult to predict, motion. Moreover, the constraints of mass conservation in a confined, incompressible, flow means that flow direction cannot be predicted just on the basis of local temperature gradients. In contrast to the evolution of temperature in these systems, fluid velocity at each location is coupled to the velocity field throughout the system. As a result, it is not necessarily the case that in all regions that the fluid motion will align in the direction of the local temperature gradient.

4. Discussion

[45] In our simple calculations of mantle flow driven by plate motion and internal buoyancy forces we find that, at depths of just a few hundred kilometers, mantle flow near convergent plate margins can significantly deviate from the direction of the overlying plate motion. Our kinematic plate experiments show that the consumption of plate material along a boundary that is not orthogonal to the direction of plate velocity can result in a rotation of the velocity vectors with increasing depth so that at mid-upper mantle depths flow in some regions is almost perpendicular to the convergent plate boundary (e.g., Figures 4c and 5c). The position of the convergent plate boundary determines the position of the cold downwelling which dominates the buoyancy field. Upper mantle flow direction becomes decreasingly influenced by plate motion and increasingly influenced by the orientation of significant buoyant features. Toroidal flow is introduced into these experiments by the shear flow component at plate boundaries, however, we find that even in the shallow mantle, flow does not align with plate movement. This observation suggests that toroidal flow introduced by plate motion does not penetrate very deep into these systems. *Gable et al.* [1991] previously showed this to be the case in lower Rayleigh number,

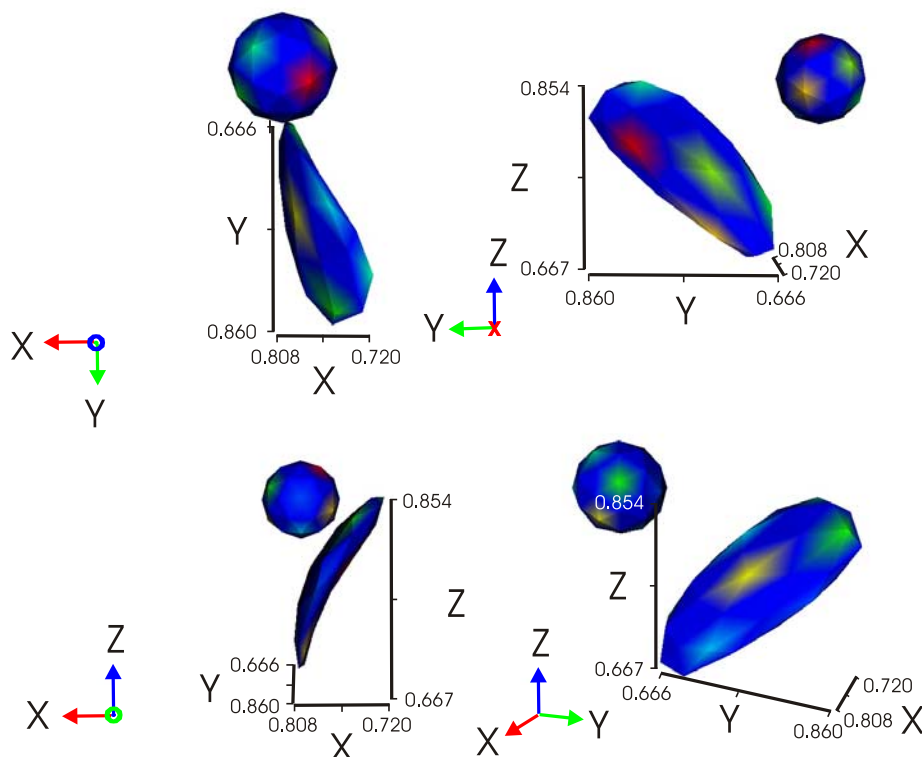


Figure 16. Before and after snapshots of the icosahedral probe placed in the time-dependent flow field of Model DTJ during the period between the snapshots shown in Figures 14 and 15. Views of the probe are shown from four different angles. The initial shape of the probe is a 42 vertex icosahedron. The final state has a flattened teardrop morphology. The figures show the relative initial and final positions of the probe. The coordinates marked on the axes shown give the locations of the probes in the $3 \times 3 \times 1$ solution domain with the origin indicated in Figure 12. The directions of the x , y , and z axes are indicated by the red, green, and blue axes, respectively. The axes color convention is consistent with previous figures. The central point of the initial icosahedron travels the trajectory shown in Figure 15. Several vertices are colored to provide reference points for the viewer. The icosahedron's initial maximum width is approximately 250 km. The deformation of the probe indicates stretching predominantly in the y and z directions of the coordinate system. Figure 15 shows that this corresponds to alignment of the long axis of the deformed probe approximately parallel to the strike of an adjacent slab.

smaller aspect ratio calculations and demonstrated that toroidal flow introduced by plate motion decays rapidly when the upper mantle is less viscous than the lower mantle.

[46] Although mantle flow is not bound to align with plate motion it is very clear that when plate velocity is comparable to the velocities driven by buoyancy, plate geometry has a significant effect on deep mantle flow by determining the position and shape of the downwelling features that dominate the buoyancy field of the systems. Moreover, the positions of downwellings largely determine the positions of upwellings and therefore the approximate planform of the system. For example, flow in Model K0 remains essentially two-dimensional in a system that would dissolve into three-dimensional short wavelength features [e.g., *Dubuffet et al.*,

2000] because of the motion of the plates and their 1D geometry. It is apparent that plate motion strongly influences convective wavelength by organizing buoyant features but its effect on local (small-scale) velocity diminishes in comparison with buoyancy at relatively shallow depths (a few hundred kilometers).

[47] Plates are also responsible for organizing the long tube-like warm anomalies that envelop the downwellings in these systems. An example of the ability of these anomalously warm pockets of material to drive lateral flow near cold downwellings is indicated in the results from Model DLT. Figure 10 shows that warm anomalies can grow stronger on one side of a downwelling than the other and that flow may be driven horizontally between large enough gaps or tears in sheet-like

downwellings by warm material trying to rise against the downward drag of the sinking cold material.

[48] One obvious way in which our models differ from mantle convection in the Earth is the limitation of static plate boundaries. While we would expect these calculations to evolve quite differently if evolving plate boundaries were incorporated in the calculation, the velocity fields calculated at the given instant have no dependence on the history of the calculation (equation (2)). The only requirement needed to reasonably compare solutions for flow in our calculations to flow in the mantle is that the temperature fields that we consider must represent the sort of temperature distributions that are expected in mantle-like systems with the corresponding plate velocities. A limitation of our calculations that will effect the results is their aspect ratio. For example, Model DTJ has a surface area that scales to approximately fifteen percent of the Earth's surface area. Consequently, a much shorter periodicity is imposed on the solutions than exists in the Earth. It is difficult to assess whether this characteristic of our study will have any significant effect on our findings. Similar studies including larger plates and a spherical geometry should be the subject of future work. The area of the plates employed in our calculations are comparable to the Earth's smaller plates.

[49] The results from Model DTJ clearly shows that flow in complex 3D, time-dependent, settings does not always follow local temperature gradients. In this calculation, flow below Plate 4 in the vicinity of the convergent boundary between Plates 3 and 4 is moving parallel to the adjacent downwelling at mid-upper mantle depths. This flow solution is possible even though temperature gradients and the dynamically determined plate velocities are the only forces driving the flow and there are no lateral variations in viscosity. In contrast to the energy equation (3), which is used to update temperature and is solved explicitly, the momentum equation (2) which determines flow from temperature must be solved implicitly. That is, considering the method of solution of these equations clarifies that in contrast to temperature, flow at all locations in the system is coupled to flow at every other point in the fluid at all times. In an incompressible fluid contained in a finite volume this means that it may be the case that flow is not always directed toward the closest sinking feature. Other remote features may be more influential. This is clearly indicated by the region where flow

is moving parallel to the downwelling sheet in Model DTJ. This surprising result occurs because local flow adjacent to one downwelling is being forced with the overall flow toward another more dominant downwelling.

[50] It is not clear, without examining hundreds of snapshots of temperature fields, whether examples of mantle flow moving parallel to a slab-like feature (as in Model DTJ) are common or whether it is a rare event consistent with only specially configured thermal fields. (For example, "Y"-junction-like configurations of downwelling sheets where the buoyancy associated with the different arms of the Y differs.) Whatever the case, Model DTJ shows that the complexity of 3D mantle convection with plates does not require upper mantle flow to always be drawn toward the nearest cold feature. Thus, in regions with complex plate geometries it may not be the case that upper-mantle flow will always move orthogonally to the closest plate boundary.

[51] Although our models are simple, they do exhibit flow features that are reminiscent of those inferred [Helffrich *et al.*, 2002; Smith *et al.*, 2001; Currie *et al.*, 2004; Klosko *et al.*, 1999] from shear-wave splitting patterns in subduction regions. Models like DTJ and DLT show transitions from trench parallel flow to trench perpendicular flow along plate boundaries. Such variability is seen in shear-wave splitting results for a number of subduction regions. Specifically upper-mantle flow in model DTJ is reminiscent of shear-wave splitting patterns in the NW Pacific. Fast shear-wave polarization directions are oblique to the Mariana and Izu-Bonin subduction zones [Fouch and Fisher, 1996, 1998]. Splitting directions are primarily trench parallel along the Ryukyu Arc [Long and van der Hilst, 2006]. At the central Japan triple junction, where the Pacific, Philippine and Eurasian plate meet, the splitting pattern becomes more complicated [Okada *et al.*, 1995; Sandvol and Ni, 1997]. North of this region near western Honshu the fast direction is roughly parallel to the trench. Toward the Kuril arc the fast-shear-wave polarizations are more N-S, oblique to the convergence direction [Sandvol and Ni, 1997; Fouch and Fischer, 1996]. Finally, even further north in the Kamchatka region, SKS polarization directions above the Benioff zone are trench parallel [Peyton *et al.*, 2001]. However, stations located away from the slab and near the Kamchatka-Aleutian junction, where the slab terminates, show trench normal orientations.

[52] The next step in this work is to do a formal LPO calculation linked to the flow modeling. Past efforts have focused on relatively simple models that are usually 2D and time invariant [e.g., *Blackman et al.*, 1996; *Tommasi*, 1998; *Chastel et al.*, 1993; *Blackman and Kendall*, 2002; *Kaminski and Ribe*, 2001; *Hall et al.*, 2000]. In our case the problem is more complicated due to the complex flow geometries revealed in our calculations.

[53] Our conclusions regarding the interpretation of shear-wave splitting in subduction environments are predicated under the assumption that the olivine *a* axes in mantle peridotites will align in the flow direction [e.g., *Ben-Ismaïl and Mainprice*, 1998]. Recent work has suggested that this may not always be the style of olivine deformation in a subduction region. It has been proposed that an olivine B-type fabric may develop in highly strained hydrous parts of the upper-mantle wedge [*Jung and Karato*, 2001] which would align the *a* axes perpendicular to the flow [*Kneller et al.*, 2006]. However, our results show that significant along-strike flow can occur deep in the upper mantle, a region unlikely to be hydrated. Recent studies of mantle anisotropy in subduction regions of the Caribbean suggest significant along-strike subslab flow (L. Pinero-Feliciangeli and J-M. Kendall, Subslab mantle flow parallel to the Caribbean plate boundaries: Inferences from SKS splitting, submitted to *Tectonophysics*, 2007). It has also been recently suggested that there may be a transition from a [100] to [001] slip direction in olivine at depths between 200–300 km [*Mainprice et al.*, 2005], which would lead to less seismic anisotropy in the region above the transition zone. Future LPO calculations should consider these effects.

5. Conclusions

[54] We have examined six 3D models of whole mantle convection incorporating finite thickness viscous plates with specified plate geometries and both specified and dynamically determined plate velocities. The systems investigated feature surface velocities of the order of cm/yr, vigorous convection at whole mantle type Rayleigh numbers and the inclusion of internal heating and depth-dependent viscosities.

[55] Introducing a two-dimensionality into the plate geometry introduces three-dimensionality into the system that is absent when a one-dimensional plate geometry is specified (e.g., Model K0). In our

calculations with kinematic plate velocities, we used experiments with varying degrees of strike-slip motion in their surface velocity to show that buoyancy-driven flow associated with the pull of downwelling sheets dominates plate-driven flow in the mid-upper mantle. Subsequently, we examined more complex scenarios and found that not only did the direction of flow in the upper mantle not necessarily correlate with the direction of motion of the overlying plate but that the positioning of buoyant features was also not a guide for the reliable prediction of surrounding mantle flow direction.

[56] In one case that we examined (Model DLT), we find that a component of lateral flow drives predominantly horizontal motion that is parallel to a downwelling sheet for a distance of a few hundred kilometers. In this model, regions exhibiting parallel to slab flow extend several hundred kilometers but only exist near the edge of the slab-like feature. This motion may be driven by broad regions below the plates where temperatures differ on opposite sides of the downwelling sheet.

[57] The calculation featuring the most complex plate geometry that we investigated (Model DTJ) also gives the most time-dependent solution. The complex configuration of downwelling features in the calculation does not allow for a flow solution where mantle motion is everywhere attracted toward the closest downwelling. Forcing determined by the most dominant downwelling in the system entrains flow below neighboring plates in a large-scale flow pattern that influences the entire system. Consequently, flow adjacent to one of the sheet-like cold anomalies in the model moves parallel to the overlying plate boundary for a period in excess of 26 Myr and a distance in excess of 2000 km. Within the region exhibiting slab parallel flow, calculations using particle trajectories show stretching and shearing of the mantle in the parallel to strike and vertical directions.

[58] We suggest that our findings may help explain the observed variations in the shear-wave fast polarization directions from seismic anisotropy studies in the Western Pacific. The network of convergent plate boundaries extending north from New Guinea to Kamchatka is characterized by findings from anisotropy studies that show little correlation between the strike of convergent plate boundaries and the fast direction for seismic wave propagation. On the basis of the findings presented here, we suggest that the interpreted flow directions inferred from anisotropy observations in the

Western Pacific may well be accurately recording regions of slab parallel flow juxtaposed with regions characterized by slab normal flow. However, we require a better understanding of the translation between the seismic observations and exact flow direction, which will come from mineral physics, seismology and geodynamical studies.

Acknowledgments

[59] Funding from NERC (NER/O/S/2001/01227) during the course of this work is gratefully acknowledged. L.T.P.F. received financial support from the Consejo de Desarrollo Científico y Humanístico del Universidad Central de Venezuela.

References

- Alvarez, W. (1992), Geological evidence for the geographical pattern of mantle return flow and the driving mechanism of plate tectonics, *J. Geophys. Res.*, **87**, 6697–6710.
- Ben-Ismaïl, W., and D. Mainprice (1998), An olivine fabric database: An overview of upper mantle fabrics and seismic anisotropy, *Tectonophysics*, **296**, 145–157.
- Blackman, D. K., and J.-M. Kendall (2002), Seismic anisotropy in the upper mantle: 2. Predictions for current plate boundary flow models, *Geochem. Geophys. Geosyst.*, **3**(9), 8602, doi:10.1029/2001GC000247.
- Blackman, D. K., J.-M. Kendall, P. Dawson, H.-R. Wenk, D. Boyce, and J. Phipps Morgan (1996), Teleseismic imaging of subaxial flow at mid-ocean ridges: Travel-time effects of anisotropic mineral texture in the mantle, *Geophys. J. Int.*, **127**, 415–426.
- Buffett, B. A. (2003), The thermal state of Earth's core, *Science*, **299**, 1675–1677.
- Busse, F. H., et al. (1993), 3D convection at infinite Prandtl number in Cartesian geometry—A benchmark comparison, *Geophys. Astrophys. Fluid Dyn.*, **75**, 39–59.
- Buttles, J., and P. Olson (1998), A laboratory model of subduction zone anisotropy, *Earth Planet. Sci. Lett.*, **164**, 245–262.
- Chastel, T. B., P. R. Dawson, H.-R. Wenk, and K. Bennett (1993), Anisotropic convection with implications for the upper mantle, *J. Geophys. Res.*, **98**, 17,757–17,771.
- Currie, C. A., J. F. Cassidy, R. D. Hyndman, and M. G. Bostock (2004), Shear wave anisotropy beneath the Cascadia subduction zone and western North American craton, *Geophys. J. Int.*, **157**, 341–353.
- Dubuffet, F., M. Rabinowicz, and M. Monnereau (2000), Multiple scales of mantle convection, *Earth Planet. Sci. Lett.*, **178**, 351–366.
- Forte, A. M., and J. X. Mitrovia (1996), New inferences of mantle viscosity from joint inversion of long-wavelength mantle convection and postglacial rebound data, *Geophys. Res. Lett.*, **23**, 1147–1150.
- Forte, A. M., and J. X. Mitrovia (2001), Deep-mantle high-viscosity flow and thermochemical structure inferred from seismic and geodynamic data, *Nature*, **410**, 1049–1056.
- Forte, A. M., and W. R. Peltier (1987), Plate tectonics and aspherical Earth structure: The importance of poloidal-toroidal coupling, *J. Geophys. Res.*, **92**, 3645–3679.
- Fouch, M. J., and K. M. Fischer (1996), Mantle anisotropy beneath northwest Pacific subduction zones, *J. Geophys. Res.*, **101**, 15,987–16,002.
- Fouch, M. J., and K. M. Fischer (1998), Shear wave anisotropy in the Mariana subduction zone, *Geophys. Res. Lett.*, **25**, 1221–1224.
- Gable, C. W., R. J. O'Connell, and B. J. Travis (1991), Convection in three dimensions with surface plates: Generation of toroidal flow, *J. Geophys. Res.*, **96**, 8391–8405.
- Hager, B. H. (1994), Subducted slabs and the geoid: Constraints on mantle rheology and flow, *J. Geophys. Res.*, **89**, 6003–6015.
- Hall, C. E., K. M. Fischer, E. M. Parmentier, and D. Blackman (2000), The influence of plate motions on three-dimensional back arc mantle flow and shear wave splitting, *J. Geophys. Res.*, **105**, 28,009–28,033.
- Helffrich, G., D. A. Wiens, E. Vera, S. Barrientos, P. Shore, S. Robertson, and R. Adaros (2002), A teleseismic shear-wave splitting study to investigate mantle flow around South America and implications for plate-driving forces, *Geophys. J. Int.*, **149**, F1–F7.
- Hofmeister, A. M. (1999), Mantle values of thermal conductivity and the geotherm from phonon lifetimes, *Science*, **283**, 1699–1706.
- Jellinek, A. M., H. M. Gonnermann, and M. A. Richards (2003), Plume capture by divergent plate motions: Implications for the distribution of hotspots, geochemistry of mid-ocean ridge basalts, and estimates of the heat flux at the core-mantle boundary, *Earth Planet. Sci. Lett.*, **205**, 361–378.
- Jung, H., and S. Karato (2001), Water-transitions in olivine, *Science*, **293**, 1460–1463.
- Kaminski, E., and N. M. Ribe (2001), A kinematic model for recrystallization and texture development in olivine polycrystals, *Earth Planet. Sci. Lett.*, **189**, 253–267.
- King, S. D., and T. G. Masters (1992), An inversion for the radial viscosity structure using seismic tomography, *Geophys. Res. Lett.*, **19**, 1551–1554.
- King, S. D., C. W. Gable, and S. A. Weinstein (1992), Models of convection-driven tectonic plates: A comparison of methods and results, *Geophys. J. Int.*, **109**, 481–487.
- King, S. D., J. P. Lowman, and C. W. Gable (2002), Episodic tectonic plate reorganizations driven by mantle convection, *Earth Planet. Sci. Lett.*, **203**, 83–91.
- Klosko, E. R., F. T. Wu, H. J. Anderson, D. Eberhart-Phillips, T. V. McEvilly, E. Audoin, M. K. Savage, and K. R. Gledhill (1999), Upper mantle anisotropy in the New Zealand region, *Geophys. Res. Lett.*, **26**, 1497–1500.
- Kneller, E. A., P. E. van Keken, S. Karato, and J. Park (2006), BD-type olivine fabric in the mantle wedge: Insights from high-resolution non-Newtonian subduction zone models, *Earth Planet. Sci. Lett.*, **237**, 781–791.
- Koglin, D. E. Jr., S. R. Ghias, S. D. King, G. T. Jarvis, and J. P. Lowman (2005), Mantle convection with reversing mobile plates: A benchmark study, *Geochem. Geophys. Geosyst.*, **6**, Q09003, doi:10.1029/2005GC000924.
- Korenaga, J., and T. H. Jordan (2004), Physics of multiscale convection in Earth's mantle: Evolution of sublithospheric convection, *J. Geophys. Res.*, **109**, B01405, doi:10.1029/2003JB002464.
- Long, M. D., and R. D. van der Hilst (2006), Shear wave splitting from local events beneath the Ryukyu arc: Trench-parallel anisotropy in the mantle wedge, *Phys. Earth Planet. Inter.*, **151**, 206–222.
- Lowman, J. P., S. D. King, and C. W. Gable (2001), The influence of tectonic plates on mantle convection patterns, temperature and heat flow, *Geophys. J. Int.*, **146**, 619–636.
- Lowman, J. P., S. D. King, and C. W. Gable (2003), The role of the heating mode of the mantle in intermittent reorganiza-

- p>tion of the plate velocity field,
- Geophys. J. Int.*
- ,
- 152**
- , 455–467.
- Lux, R. A., G. F. Davies, and J. H. Thomas (1979), Moving lithosphere plates and mantle convection, *Geophys. J. R. Astron. Soc.*, **57**, 209–228.
- Mainprice, D., A. Tommasi, H. Couvy, P. Cordier, and D. J. Frost (2005), Pressure sensitivity of olivine slip systems: Implications for the interpretation of seismic anisotropy of the Earth's upper mantle, *Nature*, **433**, 731–733.
- Mitrovica, J. X., and A. M. Forte (2004), A new inference of mantle viscosity based upon joint inversion of convection and glacial isostatic adjustment data, *Earth Planet. Sci. Lett.*, **225**, 177–189.
- Okada, T., T. Matsuzawa, and A. Hasegawa (1995), Shear wave polarization anisotropy beneath the northeastern part of Honshu, Japan, *Geophys. J. Int.*, **123**, 781–797.
- Peyton, V., V. Levin, J. Park, M. Brandon, J. Lees, E. Gordeev, and A. Ozerov (2001), Mantle flow at a slab edge: Seismic anisotropy in the Kamchatka region, *Geophys. Res. Lett.*, **28**, 379–382.
- Pysklywec, R. N., and J. X. Mitrovica (1997), Mantle avalanches and the dynamic topography of continents, *Earth Planet. Sci. Lett.*, **148**, 447–455.
- Ribe, N. M. (1989), Seismic anisotropy and mantle flow, *J. Geophys. Res.*, **94**, 4213–4223.
- Ricard, Y., L. Fleitout, and C. Froidevaux (1984), Geoid heights and lithospheric stresses for a dynamic Earth, *Ann. Geophys.*, **2**, 267–286.
- Richards, M. A., and B. H. Hager (1984), Geoid anomalies in a dynamic Earth, *J. Geophys. Res.*, **89**, 5987–6002.
- Richter, F. M. (1973), Convection and large-scale circulation of the mantle, *J. Geophys. Res.*, **78**, 8735–8745.
- Richter, F. M., and B. Parsons (1975), On the interaction of two scales of convection in the mantle, *J. Geophys. Res.*, **80**, 2529–2541.
- Russo, R. M., and P. G. Silver (1994), Trench parallel flow beneath the Nazca from seismic anisotropy, *Science*, **263**, 1105–1111.
- Sabadini, R., and D. A. Yuen (1989), Mantle stratification and long-term polar wander, *Nature*, **339**, 373–375.
- Sandvol, E., and J. Ni (1997), Deep azimuthal anisotropy in the southern Kurile and Japan subduction zones, *J. Geophys. Res.*, **102**, 9911–9922.
- Savage, M. K. (1999), Seismic anisotropy and mantle deformation: What have we learned from shear wave splitting?, *Rev. Geophys.*, **37**, 65–106.
- Smith, G. P., D. A. Wiens, K. M. Fischer, L. M. Dorman, S. C. Webb, and J. A. Hildebrand (2001), A complex pattern of mantle flow in the Lau backarc, *Science*, **292**, 713–716.
- Spada, G., Y. Ricard, and R. Sabadini (1992), Excitation of true polar wander by subduction, *Nature*, **360**, 452–454.
- Stacey, F. D. (1992), *Physics of the Earth*, 3rd ed., Brookfield, Brisbane, Australia.
- Tommasi, A. (1998), Forward modelling of the development of seismic anisotropy in the upper mantle, *Earth Planet. Sci. Lett.*, **160**, 1–13.
- Travis, B., C. J. Anderson, J. Baumgardner, C. W. Gable, B. H. Hager, R. J. O'Connell, P. Olson, A. Raefsky, and G. Schubert (1991), A benchmark comparison of numerical methods for infinite Prandtl number thermal convection in two-dimensional Cartesian geometry, *Geophys. Astrophys. Fluid Dyn.*, **55**, 137–160.
- van Hunen, J., J. Huang, and S. Zhong (2003), The effect of shearing on the onset and vigor of small-scale convection in a Newtonian rheology, *Geophys. Res. Lett.*, **30**(19), 1991, doi:10.1029/2003GL018101.
- van Keken, P. E., and C. W. Gable (1995), The interaction of a plume with a rheological boundary: A comparison between two- and three-dimensional models, *J. Geophys. Res.*, **100**(B10), 20,291–20,302.
- van Keken, P. E., and S. Zhong (1999), Mixing in a 3D spherical model of present-day mantle convection, *Earth Planet. Sci. Lett.*, **171**, 533–547.
- Yu, Y., and J. Park (1994), Hunting for azimuthal anisotropy beneath the Pacific Ocean region, *J. Geophys. Res.*, **99**, 15,399–15,421.
- Zhang, S., and S. Karato (1995), Lattice preferred orientation of olivine aggregates deformed in simple shear, *Nature*, **375**, 774–777.